water

MDPI

Article

Injection of zerovalent iron gels for aquifer nanoremediation: lab experiments and modeling

Federico Mondino[1], Amelia Piscitello[1], Carlo Bianco[1], Andrea Gallo[1], Alessandra de Folly D'Auris[2], Tiziana Tosco[1], Marco Tagliabue[2] and Rajandrea Sethi[1]*

[1] Department of Environment, Land and Infrastructure Engineering, Politecnico di Torino, corso Duca degli Abruzzi 24, 10129 Torino, Italy; federico.mondino@polito.it (F.M.); amelia.piscitello@polito.it (AP); carlo.bianco@polito.it (C.B.); andrea.gallo@polito.it (A.G.); tiziana.tosco@polito.it (T.T.), rajandrea.sethi@polito.it (R.S.)

[2] Decarbonisation and Environmental Laboratories, Eni S.p.A., Via F. Maritano 26, 20097 San Donato M.se, Italy; alessandra.de.folly.dauris@eni.com (A.D.); marco.tagliabue@eni.com (M.T.)

* Correspondence: rajandrea.sethi@polito.it (R.S.); Tel.: +39-0110907735

Received: date; Accepted: date; Published: date

Supplementary Material

1. Rheology of the gel inside the porous medium

The rheology of the gel inside the porous medium was characterized following the same procedure applied in Gastone, *et al.* [1]:

- 4 column tests of slurry transport were performed at different discharge rates and the variation of pressure drop over time was recorded (Figure S 1);
- the test-specific dynamic viscosity μ_m [ML^{-1}T^{-1}] was calculated applying the Darcy law generalized for non-Newtonian fluids:
$$\mu_m = \frac{k}{q}\frac{\Delta P'}{L}$$
where q is the applied flow velocity q [LT^{-1}], k is the porous medium permeability [L^2], L is the length of the column [L] and ΔP′ is the pressure drop measured after 1 pore volume (PV) from the beginning of the particle injection [MLT^{-2}];
- a shear rate value ($\dot{\gamma_m}$) is calculated for each test with the following equation:
$$\dot{\gamma_m} = \alpha \frac{q}{\sqrt{K\varepsilon}}$$
where ε is the porous medium porosity and α is the shift factor, which is initially assumed equal to 1. These data of shear rates ($\dot{\gamma_m}$) and viscosities in the porous medium ($\mu_m(\dot{\gamma_m})$), reported in Table S 1, constitute the fluid rheogram in the porous medium.
- the final shift factor value is estimated by overlapping the fluid rheograms in the porous medium and in the bulk. In this study, a shift factor of 1 was sufficient to guarantee a satisfying match of the two curves.

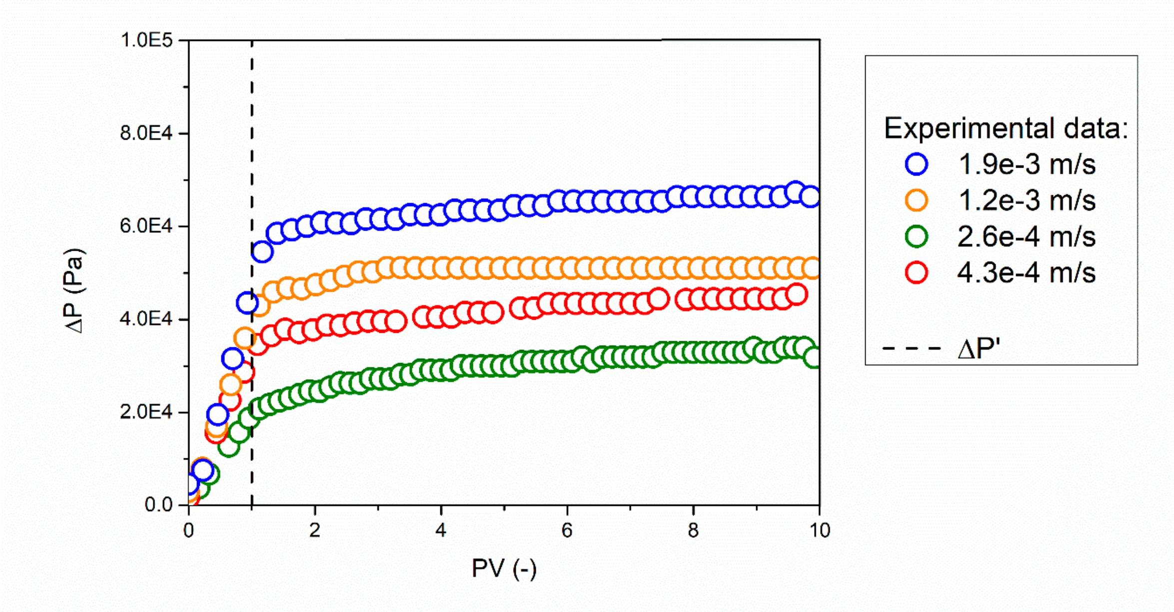

Figure S 1 - Pressure drop over time recorded for the column transport tests of mZVI particles at different discharge rates. The dashed line indicates the time at which the pressure drop was measured to determine the gel dynamic viscosity μ_m.

Table S 1 - Shear rate ($\dot{\gamma}_m$) *and viscosities in the porous medium* ($\mu_m(\dot{\gamma}_m)$)

Test	$\dot{\gamma}_m$ **(s^{-1})**	$\mu_m(\dot{\gamma}_m)$ **(Pa · s)**
q_1	31.3	$3.29 \cdot 10^{-2}$
q_2	56.4	$2.83 \cdot 10^{-2}$
q_3	141.0	$1.57 \cdot 10^{-2}$
q_4	218.2	$1.30 \cdot 10^{-2}$

2. MZVI transport in 1D geometries: model and column test interpretation

The experimental data of the column transport tests are shown in

Figure S 2 in terms of breakthrough curves, total iron concentration profiles and pressure build-up. The breakthrough curves of each test follow a similar pattern and highlight the achievement of an overall good mobility of mZVI particles in the porous medium. The first step of the injection looks similar in all the tests, indicating that the different velocities do not substantially affect the slurry transport in the shorter times. The particle arrival time is close to what expected for a tracer (around 1 PV), suggesting that no equilibrium adsorption phenomena are taking place. After the first pore volume of injection, the outlet particle concentration keeps rising with a slight steepness and the breakthrough curve takes a sigmoidal form, suggesting the reduction of the particle deposition rate, which is typical of the blocking retention mechanism [2]. The second part of the curves is levelled off and approach an almost asymptotic value, meaning that a steady state outlet concentration is reached. However, despite the asymptotic value is considerably high (above 80% in each test), it is always lower than one ($C/C_0 < 1$), indicating that the particles irreversible filtration is taking place. The total iron concentration profiles show the typical shape of strained deposits, confirming the presence of the second interaction site of irreversible straining [3,4]. Looking at the graph of the pressure drop along the column (

Figure S 2 c), the data show an increase of the pressures with the rise of the flow velocity employed for the test. However, the growth is not linear due to the fluid non-Newtonian nature, thus the velocity rise is partly counterbalanced by the viscosity reduction (in accordance with the shear-thinning behaviour of the XG/GG mixture).

The column transport tests results were interpreted by means of the numerical tool MNMs 2018 (https://areeweb.polito.it/ricerca/groundwater/software/mnms/). For one-dimensional problems, the MZVI transport was modelled with the following modified advection-dispersion equation [4,5]:

$$\begin{cases} \dfrac{\partial(\varepsilon C_{Fe})}{\partial t} + \sum \dfrac{\partial(\rho_b S_{Fe,i})}{\partial t} + \dfrac{\partial(q C_{Fe})}{\partial x} - \dfrac{\partial}{\partial x}\left[\varepsilon D \dfrac{\partial C_{Fe}}{\partial x}\right] = 0 \\ \dfrac{\partial(\rho_b S_{Fe,1})}{\partial t} = \varepsilon k_{a1}\left(1 - \dfrac{S_{Fe,1}}{S_{max}}\right) C \\ \dfrac{\partial(\rho_b S_{Fe,2})}{\partial t} = \varepsilon k_{a2}\left[\dfrac{d_{50,sand} + x}{d_{50,sand}}\right]^{-\beta_{str}} C_{Fe} \end{cases} \tag{S1}$$

where C_{Fe} is the particle concentration in the liquid phase $[ML^{-3}]$, $S_{Fe,i}$ is the concentration in the solid phase $[-]$, ρ_b is the bulk density of the porous medium $[ML^{-3}]$, ε is the porosity [-], q is the Darcy velocity $[LT^{-1}]$, D is the hydrodynamic dispersion coefficient $[L^2T^{-1}]$, $k_{a,1}$ and $k_{a,2}$ are the particle attachment rate coefficients $[T^{-1}]$, S_{max} is the maximum concentration of deposited particles $[-]$, $d_{50,sand}$ is the median grain size of the porous medium and β_{str} is the exponent coefficient defining the interaction dynamics $[-]$.

Two concurrent interaction sites (i=1, 2) for two different process were considered:

- First site expressing irreversible blocking dynamics;
- Second site expressing irreversible straining phenomena.

The flow velocity and the fluid viscosity affect the transport of the particles and the attachment kinetics, $k_{a,i}$ can be expressed as [6,7]:

$$k_{a,i}(v) = C_{a,i}\frac{q}{\varepsilon d_{50,sand}}\eta_0$$

where $C_{a,i}$ is the coefficient to be determined from the fitting of the experimental data, η_0 is the single collector efficiency. For calculation of η_0, an additivity assumption is considered to take into account the contribution of three different deposition mechanisms [8]:

$$\eta_0 = \eta_G + \eta_I + \eta_D$$

where:

η_G is the single collector efficiency due to the sedimentation;

η_I is the single collector efficiency due to the interception;

η_D is the single collector efficiency due to the Brownian diffusion.

There are several formulations for calculating the terms composing the *single collector efficiency* η_0. In this work, the formulation from Yao et al. [9] was chosen because of its simplicity:

$$\eta_I = \frac{3}{2}\left(\frac{d_{50,p}}{d_{50,sand}}\right)^2$$

$$\eta_D = 4.04 Pe^{-\frac{2}{3}}$$

$$\eta_G = \frac{v_s}{q}$$

where:

$d_{50,p}$ is the average diameter of the colloidal particles $[L]$;

Pe is the Peclet number, that is a measure of the relative importance of advection versus diffusion [10]. Pe depends both on the flow field velocity and on a characteristic length of the system [11] $[-]$;

v_s is the sedimentation rate of the particle in the pore fluid $[LT^{-1}]$.

For each column test, one set of velocity-dependent attachment coefficients $k_{a,1}$ and $k_{a,2}$ and a straining parameter β_{str} were determined by experimental data fitting. Table S 2 reports the parameters $k_{a,1}$, $k_{a,2}$, β_{str} obtained from the fitting. The blocking parameter S_{max} was instead assumed constant for all the tests and equal to 0.0027 (-).

The model correctly reproduced the pattern of all the experimental data, both in terms of shape and arrival time, thus confirming the correctness of the hypothesis made about the transport mechanisms: two different interaction sites of irreversible blocking (site 1) and irreversible straining (site 2).

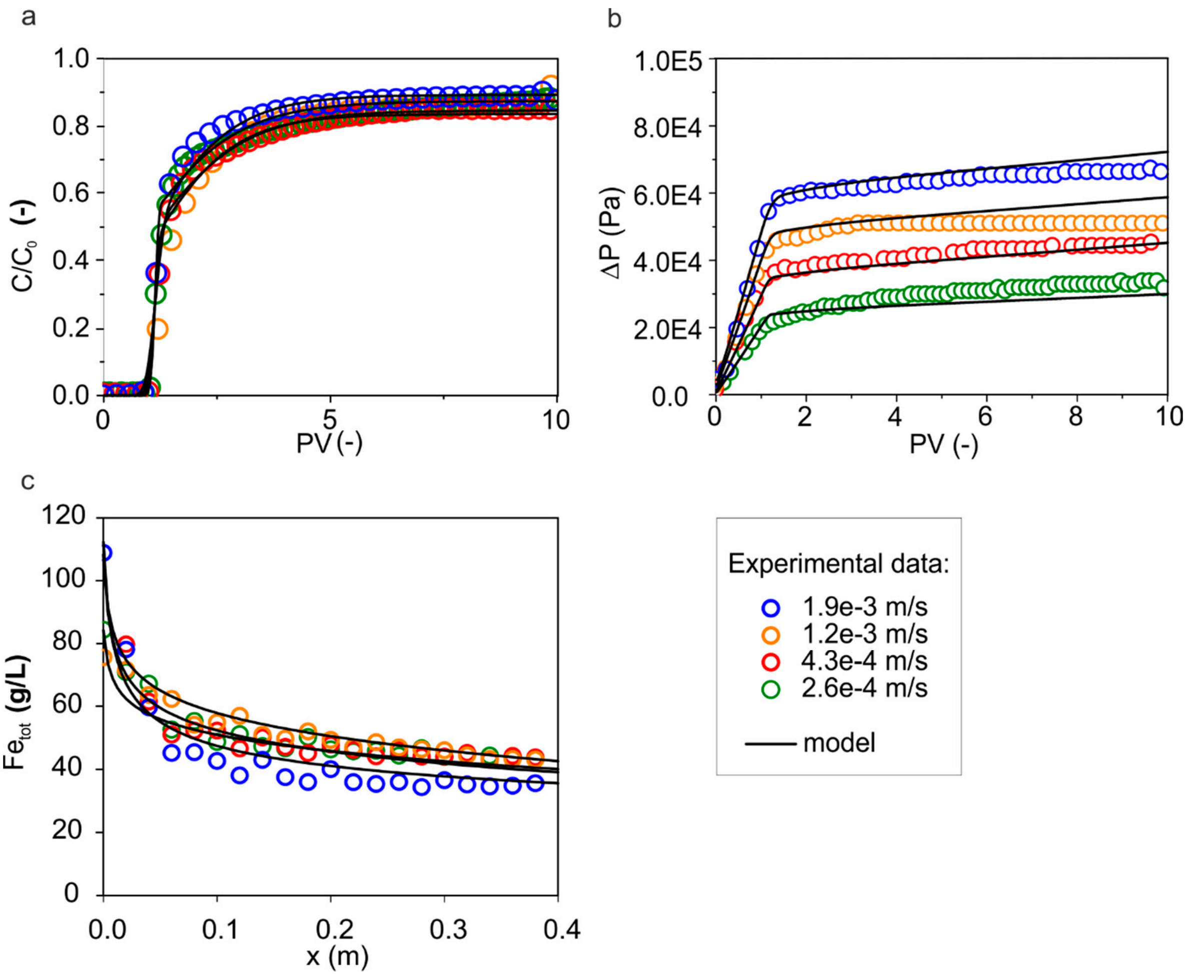

Figure S 2 - Breakthrough curves, iron concentration profiles and pressure drop along the column for the transport test of mZVI particles at 20 g/L stabilized with the shear thinning gel at a concentration of 1.75 g/L. Test are performed at different velocities. Experimental data are reported as points, while black lines indicates the modelled curves.

Table S 2 – Transport and clogging parameters obtained through the fitting of the column transport test for mZVI at 20 g/L dispersed in GG/XG at 1.75 g/L at different velocities.

Test	**q (m/s)**	**η_0 (-)**	**$k_{a,1}$ (s^{-1})**	**$k_{a,2}$ (s^{-1})**	**β_{str} (-)**
q1	$1.10 \cdot 10^{-4}$	$2.94 \cdot 10^{-3}$	$6.77 \cdot 10^{-4}$	$7.00 \cdot 10^{-4}$	0.21
q2	$4.30 \cdot 10^{-4}$	$2.79 \cdot 10^{-3}$	$1.40 \cdot 10^{-3}$	$1.83 \cdot 10^{-3}$	0.23
q3	$1.20 \cdot 10^{-3}$	$2.47 \cdot 10^{-3}$	$3.70 \cdot 10^{-3}$	$6.00 \cdot 10^{-3}$	0.30
q4	$1.88 \cdot 10^{-3}$	$2.37 \cdot 10^{-3}$	$5.67 \cdot 10^{-3}$	$6.00 \cdot 10^{-3}$	0.43

Figure S 3 shows $k_{a,1}$ and $k_{a,2}$ reported as a function of $\frac{v_e}{d_{50,sand}}\eta_0$, while β_{str} is expressed as a function of v_e. A clear linear trend for the two attachment parameters was found, while the coefficient β_{str} increases exponentially with the growth of the effective velocity.

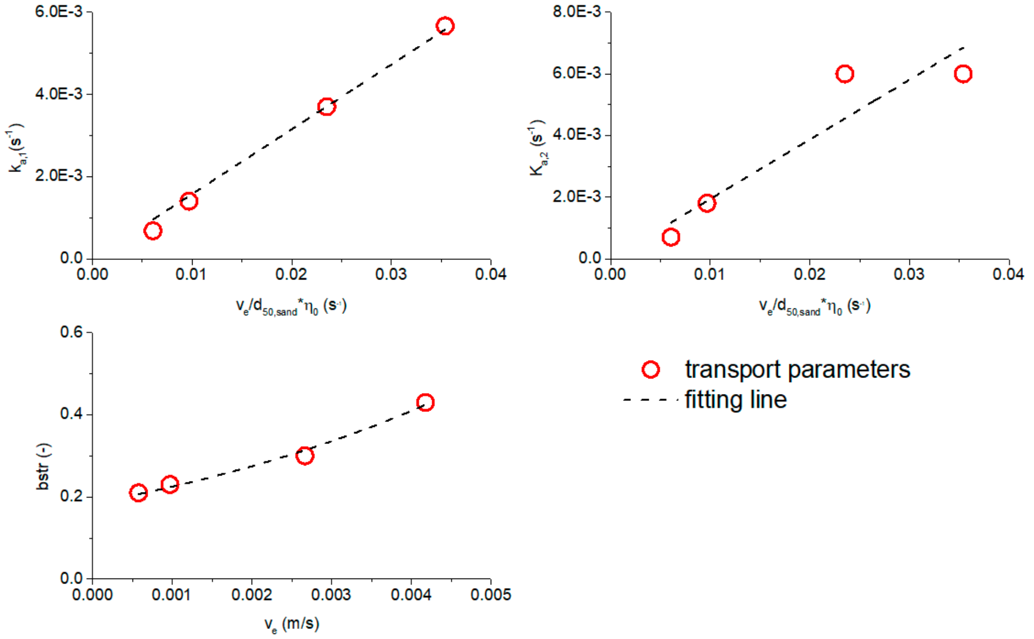

Figure S 3 - Attachment (a) coefficient for irreversible blocking (site 1), attachment (b) and β_{str} (c) coefficients for irreversible straining (site 2): obtained from the fitting of the column transport test for mZVI at 20 g/L dispersed in GG/XG at 1.75 g/L at different velocities.

3. Guar gum column filtration test

The dissolution of the guar gum powder was achieved applying the following procedure: the guar gum powder was dissolved in deionized water at 60°C and stirred for 30 minutes. After overnight hydration and sedimentation in the fridge, the supernatant was filtered through a porous medium to remove the undissolved microgels that can induce porous medium clogging. The effectiveness of this preparation method against clogging was assessed by means of filtration tests. The single-step filtration tests were performed at a constant flowrate of $8.5 \cdot 10^{-7}\ m^3/s$, which correspond to a Darcy velocity of $1.88 \cdot 10^{-3}\ m/s$. The test was divided into two steps:

- preconditioning with water: 5 PV;
- injection of the biopolymer mixture: 10 PV.

Figure S 4 shows the results obtained during the injection phase. In particular, the graph reports the pressure drop at the column end ΔP as a function of time expressed in terms of pore volume injected according to:

$$PV = \frac{t \cdot Q}{V \cdot \varepsilon}$$

where t is the time (s), Q it is the discharge (m^3/s), ε it is the porosity of the medium (-) and V is the volume of the column (m^3).

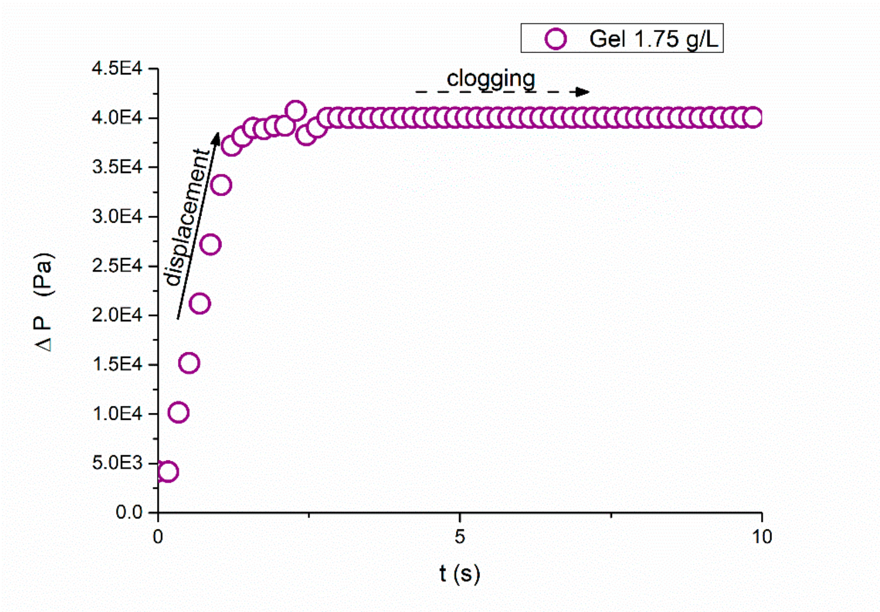

Figure S 4 - Pressure drop along the column for the gel filtration test (1.75 g/L). The black arrow indicates the increase of the pressures due to the water displacement along the column by the biopolymer solution, the dashed arrow indicates the pressure increase due to the porous medium clogging.

At the beginning of the injection phase, the pressure rises linearly due to the water displacement along the column by the biopolymer solution characterized by higher viscosity with respect to water (larger viscosity corresponds to higher pressure drop). After the first PV, the pressure remains almost constant, indicating that no clogging of the porous medium is occurring. The gel preparation procedure proved therefore effective in the removal of undissolved microgels. As a consequence the contribution of residual polymeric particle filtration to porous medium clogging was not included in the model.

4. Radial model parameters for mZVI particles stabilized with guar gum.

A radial simulation was run assuming the transport and clogging parameters for the injection of mZVI particles dispersed in 3 g/L of guar gum previously found by Tosco, Gastone and Sethi [6]. The simulation was performed using the same conditions of the radial experimental transport tests: mZVI particle concentration of 20 g/L, well radius of 0.02 m and discharge rate of 1 m^3/h for a total injection of 46 minutes.

The following model was used by Tosco, Gastone and Sethi [6] to simulate the radial transport of mZVI particles stabilized with guar gum:

$$\begin{cases} \frac{\partial \varepsilon C}{\partial t} + \sum \frac{\partial(\rho_b S_i)}{\partial t} + \frac{1}{r}\frac{\partial}{\partial r}(rqC) - \frac{1}{r}\frac{\partial}{\partial r}\left[r\varepsilon D_r \frac{\partial C}{\partial r}\right] = 0 \\ \frac{\partial(\rho_b S_1)}{\partial t} = \varepsilon k_{a1}(1 + A S_1^B)C \\ \frac{\partial(\rho_b S_2)}{\partial t} = \varepsilon k_{a2} C - \rho_b k_{d2} S_2 \end{cases}$$

Two concurrent interaction sites (i=1, 2) were considered:

- First site expressing irreversible ripening dynamics;
- Second site expressing reversible linear attachment phenomena.

Table S 3 shows the transport and clogging parameters implemented into the radial model.

Table S 3 – Model parameter implemented in the radial model [6]

Model transport parameters					Clogging parameters	
$C_{a,1}$ (s⁻¹)	A (-)	B (-)	$C_{a,2}$ (-)	$C_{d,2}$ (s·kg⁻¹)	λ (-)	ϑ (-)
0.78	11	0.61	2.01	31.35	0.45	0.36

The rheological behaviour of the GG solution was described by the Cross model [12]:

$$\begin{cases} \mu(\dot{\gamma}) = \mu_\infty + \dfrac{\mu_0 - \mu_\infty}{1 + (\lambda\dot{\gamma})^\chi} \\ \dot{\gamma_m} = \alpha \dfrac{q}{\sqrt{K\varepsilon}} \end{cases} \quad (2)$$

where:

μ is the fluid viscosity $[ML^{-1}T^{-1}]$ at a specific shear rate $\dot{\gamma}$ $[T^{-1}]$;

μ_0 is the Newtonian viscosity at low shear rate $[ML^{-1}T^{-1}]$;

μ_∞ is the Newtonian viscosity at high shear rate $[ML^{-1}T^{-1}]$;

λ is the time constant and is the shear rate reciprocal when the shear thinning behaviour starts $[T]$

χ is the model exponent $[-]$ that measures the dependence of the viscosity on the shear rate [1].

Table S 4 shows the cross parameters implemented in the radial model for the injection simulation of mZVI particles stabilized with GG solution at 3 g/L.

Table S 4 - Cross parameters of bulk viscosity curves from [1].

GG concentration (g/L)	μ_0 (Pa s)	μ_∞ (Pa s)	λ (s)	χ (-)
3	0.167	$3.42 \cdot 10^{-3}$	$5.61 \cdot 10^{-2}$	0.68

5. Tracer test in the radial setup

Before the injection test of mZVI particles into the radial model, a tracer test with bromophenol blue (BPB) at 50 mg/L was performed for a proper interpretation of the results. An injection flowrate of 7 L/h was applied following two sequential steps:

- BPB injection step of 3000 seconds for a total injected volume of 6 litres;
- water flushing of 600 seconds for a total injected volume of 1 litre.

The tracer test allowed to verify the absence of areas with different compaction in the porous medium and the determination of the hydrodynamic parameters, which are porosity ε [-] and dispersivity α_r [L]. A numerical 3D model was built using the software Visual Modflow (Waterloo Hydrogeologic Inc) for a quantitative analysis of the results. The resolution of the flow and transport problems was obtained through the numerical codes Modflow 2005 (Harbaugh 2005) and MT3DMS (Zheng and Wang 1999). The simulation results were compared to the high-resolution images captured every 30s during the tracer test.

The porosity and dispersivity values were obtained from a comparison between the experimental tracer test and the simulation performed in Visual Modflow (Figure S 5): the good overlap confirmed the correctness of the parameter estimated.

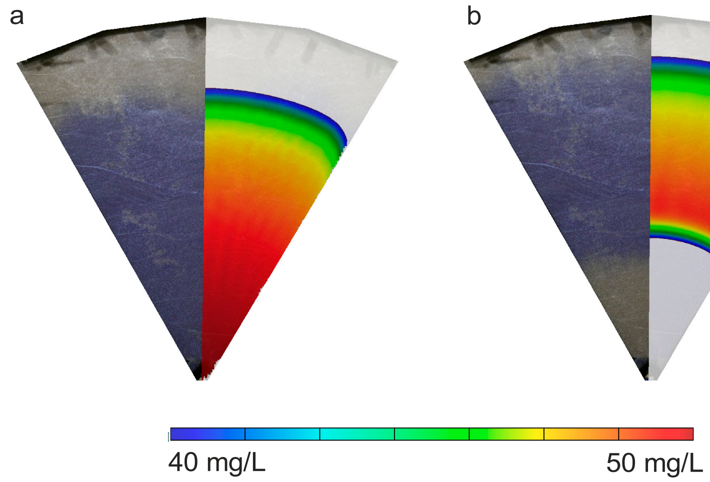

Figure S 5 - Radial tracer test with BPB at 50 mg/L and Modflow simulation: a) at the end of the injection step (3000 seconds) and b) at the end of the flushing step (3600 seconds).

6. Time evolution of the radial transport test

Figure S 6 shows the time evolution of the mZVI slurry injection into the radial model and highlight its fairly homogeneous advancement, thus confirming the proper design of the experimental setup towards the establishment of a radial flow.

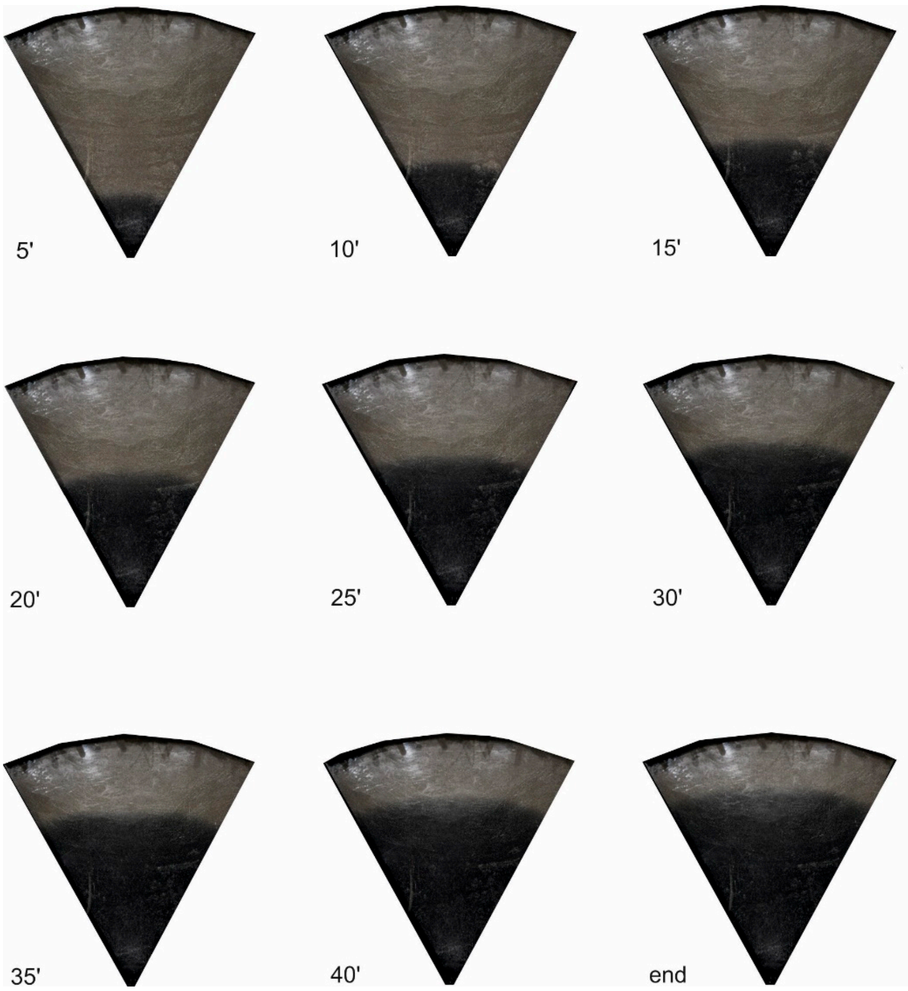

Figure S 6 – Time evolution of the injection of mZVI at 20 g/L dispersed in polymeric gel at 1.75 g/L

7. References

1. Gastone, F.; Tosco, T.; Sethi, R. Guar gum solutions for improved delivery of iron particles in porous media (Part 1): Porous medium rheology and guar gum-induced clogging. *Journal of Contaminant Hydrology* **2014**, *166*, 23-33, doi:10.1016/j.jconhyd.2014.06.013.
2. Ko, C.; Elimelech, M. The "shadow effect" in colloid transport and deposition dynamics in granular porous media: Measurements and mechanisms. *Environmental Science & Technology* **2000**, *34*, 3681-3689, doi:10.1021/es0009323.
3. Bradford, S.; Yates, S.; Bettahar, M.; Simunek, J. Physical factors affecting the transport and fate of colloids in saturated porous media. *Water Resources Research* **2002**, *38*, doi:10.1029/2002WR001340.
4. Tosco, T.; Sethi, R. Transport of Non-Newtonian Suspensions of Highly Concentrated Micro- And Nanoscale Iron Particles in Porous Media: A Modeling Approach. *Environmental Science & Technology* **2010**, *44*, 9062-9068, doi:10.1021/es100868n.
5. Bianco, C.; Tosco, T.; Sethi, R. A 3-dimensional micro- and nanoparticle transport and filtration model (MNM3D) applied to the migration of carbon-based nanomaterials in porous media. *Journal of Contaminant Hydrology* **2016**, *193*, 10-20, doi:10.1016/j.jconhyd.2016.08.006.
6. Tosco, T.; Gastone, F.; Sethi, R. Guar gum solutions for improved delivery of iron particles in porous media (Part 2): Iron transport tests and modeling in radial geometry. *Journal of Contaminant Hydrology* **2014**, *166*, 34-51, doi:10.1016/j.jconhyd.2014.06.014.
7. Litter, M. *Iron Nanomaterials for Water and Soil Treatment*; 2018; 10.1201/b22501.
8. Kretzschmar, R.; Borkovec, M.; Grolimund, D.; Elimelech, M. Mobile subsurface colloids and their role in contaminant transport. *Advances in Agronomy, Vol 66* **1999**, *66*, 121-193, doi:10.1016/S0065-2113(08)60427-7.
9. Yao, K.-M.; Habibian, M.T.; O'Melia, C.R. Water and waste water filtration. Concepts and applications. *Environ Sci Technol* **1971**, *5*, 1105-1112, doi:10.1021/es60058a005.
10. Elderfield, H.; Holland, H.D.; Turekian, K.K. *The Oceans and Marine Geochemistry*; Elsevier Science: 2006.
11. Rapp, B.E. Chapter 9 - Fluids. In *Microfluidics: Modelling, Mechanics and Mathematics*, Rapp, B.E., Ed. Elsevier: Oxford, 2017; https://doi.org/10.1016/B978-1-4557-3141-1.50009-5pp. 243-263.
12. Cross, M. Rheology of non-Newtonian fluids: a new flow equation for pseudo-plastic systems. *Journal of Colloid Science* **1965**, *20*, 417-437.